7-2015

# The sizes of candidate z~9-10 galaxies : confirmation of the bright CANDELS sample and relation with luminosity and mass.

Benne W. Holwerda
*University of Louisville*

R. J. Bouwens
*Leiden University*

P. A. Oesch
*Yale University*

R. Smit
*Leiden University*

G. D. Illingworth
*University of California, Santa Cruz*

*See next page for additional authors*

Authors

Benne W. Holwerda, R. J. Bouwens, P. A. Oesch, R. Smit, G. D. Illingworth, and I. Labbe

# THE SIZES OF CANDIDATE $z \sim 9-10$ GALAXIES: CONFIRMATION OF THE BRIGHT CANDELS SAMPLE AND RELATION WITH LUMINOSITY AND MASS

B. W. HOLWERDA[1], R. BOUWENS[1], P. OESCH[2], R. SMIT[1], G. ILLINGWORTH[3], AND I. LABBÉ[1]

[1] Leiden Observatory, Leiden University, P.O. Box 9513, 2300 RA Leiden, The Netherlands; holwerda@strw.leidenuniv.nl
[2] Yale Center for Astronomy and Astrophysics, Yale University, New Haven, CT 06520, USA
[3] UCO/Lick Observatory, University of California, Santa, Cruz, CA 95064, USA

## ABSTRACT

Recently, a small sample of six $z \sim 9$–10 candidates was discovered in CANDELS that are $\sim 10-20\times$ more luminous than any of the previous $z \sim 9$–10 galaxies identified over the HUDF/XDF and CLASH fields. We measure the sizes of these candidates to map out the size evolution of galaxies from the earliest observable times. Their sizes are also used to provide a valuable constraint on whether these unusual galaxy candidates are at high redshift. Using galfit to derive sizes from the CANDELS $F160W$ images of these candidates, we find a mean size of $0\farcs13 \pm 0\farcs02$ (or $0.5 \pm 0.1$ kpc at $z \sim 9$–10). This handsomely matches the 0.6 kpc size expected extrapolating lower-redshift measurements to $z \sim 9$–10, while being much smaller than the $0\farcs59$ mean size for lower-redshift interlopers to $z \sim 9$–10 photometric selections lacking the blue IRAC color criterion. This suggests that source size may be an effective constraint on contaminants from $z \sim 9$–10 selections lacking IRAC data. Assuming on the basis of the strong photometric evidence that the Oesch et al. sample is entirely at $z \sim 9$–10, we can use this sample to extend current constraints on the size–luminosity, size–mass relation, and size evolution of galaxies to $z \sim 10$. We find that the $z \sim 9$–10 candidate galaxies have broadly similar sizes and luminosities as $z \sim 6$–8 counterparts with star formation rate surface densities in the range of $\Sigma_{\mathrm{SFR}} = 1-20 \, M_\odot \, \mathrm{yr}^{-1} \, \mathrm{kpc}^{-2}$. The stellar mass–size relation is uncertain, but shallower than those inferred for lower-redshift galaxies. In combination with previous size measurements at $z = 4$–7, we find a size evolution of $(1 + z)^{-m}$ with $m = 1.0 \pm 0.1$ for $>0.3L*_{z=3}$ galaxies, consistent with the evolution previously derived from $2 < z < 8$ galaxies.

*Key words:* galaxies: evolution – galaxies: fundamental parameters – galaxies: high-redshift – galaxies: structure

## 1. INTRODUCTION

The installation of the WFC3/IR camera on the *Hubble Space Telescope* (*HST*) has revolutionized the search for high-redshift ($z > 6$) galaxies. At present, some $\gtrsim 800$ $z = 6-8$ galaxies are known (Bouwens et al. 2014), from deep, wide-area searches over the Hubble UltraDeep Field (HUDF, Beckwith et al. 2006), the WFC3 Early Release Survey (ERS, Windhorst et al. 2011), the CANDELS project (Grogin et al. 2011; Koekemoer et al. 2011), and the Brightest of Reionizing Galaxies (BoRG, Trenti et al. 2011, 2012; Bradley et al. 2012; Trenti 2012) fields.

The high-redshift frontier has now moved to $z \sim 9$–10, with a dozen high-fidelity candidates known (Bouwens et al. 2011a, 2011b, 2013; Zheng et al. 2012; Coe et al. 2013; Ellis et al. 2013; Oesch et al. 2013a, 2014). These highest redshift candidates can be identified by their extremely red near-infrared colors ($J - H > 0.5$), a lack of flux in bluer bands, and blue $H - 4.5\,\mu$m colors. The first $z \sim 9$–10 candidates were found both behind lensing clusters (e.g., Zheng et al. 2012; Coe et al. 2013), and in ultra-deep WFC3/IR observations (Bouwens et al. 2011a; Ellis et al. 2013; Oesch et al. 2013a).

While most of the initial $z \sim 9$–10 candidates were intrinsically very faint, Oesch et al. (2014) recently discovered a small sample of bright galaxy candidates over the CANDELS North and South. Remarkably, the Oesch et al. (2014) candidates had luminosities that were some $10$–$20\times$ brighter than the candidates discovered over the HUDF/XDF or behind lensing clusters, potentially raising questions about their high-redshift nature and whether the candidates are actually at $z \sim 9$–10.

One way of testing the high-redshift nature of these candidates is by measuring their sizes and comparing these sizes against expectations for luminous galaxy candidates at $z \sim 9$–10, as well as the sizes of potential interlopers to $z \sim 9$–10 selections. The analytical models from Fall & Efstathiou (1980) and Mo et al. (1998) predict effective radii should scale with redshift somewhere between $(1 + z)^{-1}$ for galaxies living in halos of fixed mass or $(1 + z)^{-1.5}$ at a fixed circular velocity. Observational evidence from earlier samples also points to such scaling relations, with some studies preferring $(1 + z)^{-1}$ (Bouwens et al. 2004, 2006; Oesch et al. 2010), some studies preferring $(1 + z)^{-1.5}$ (Ferguson et al. 2004), and some studies lying somewhere in between (Hathi et al. 2008; Ono et al. 2013; Shibuya et al. 2015).[4] For a comprehensive overview of the size relations of galaxies observed with *HST*, we refer the reader to Shibuya et al. (2015).

While clearly the strongest evidence for the bright candidates from Oesch et al. (2014) being at $z \sim 9$–10 would seem to be from the photometric constraints, a measurement of their sizes can serve as a useful sanity check on their high-redshift nature. Such tests are useful given the history of the former $z \sim 10$ candidate UDFj-39546284 identified in the HUDF09 observations (Bouwens et al. 2011c), but which subsequent data suggests is more likely an extreme emission-line galaxy at $z \sim 2$ based on the non-detection of the candidate in the $JH_{140}$

---

[4] After submission of this manuscript another analysis appeared on the arXiv, Curtis-Lake et al. (2014), which claims to find no evidence for evolution in galaxy sizes across $z = 4$–8. This seems to be in tension with all of the previous literature and is also inconsistent with the recent studies by Kawamata et al. (2014) and Shibuya et al. (2015) and what is found from stacking ultra-deep observations of galaxies (see Figure 22 in Bouwens et al. 2014).
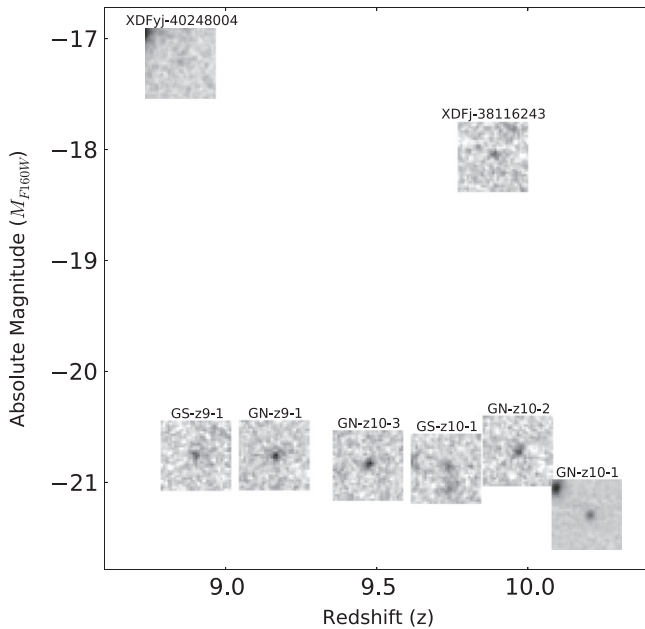
**Figure 1.** *F160W* cutouts of our eight $z \sim 9$–10 candidate galaxies presented as a function of their respective redshifts and absolute magnitudes to highlight the separation in luminosity between current CANDELS and XDF samples.

observations (Bouwens et al. 2013; Ellis et al. 2013) and the tentative detection of an emission line at ~1.6 $\mu$m (Brammer et al. 2013).

Additionally, assuming on the basis of the strong photometric evidence that the Oesch et al. (2014) candidates are indeed all bona-fide $z \sim 9$–10 galaxies (Figure 1), the luminosity and redshift of the sources provide the opportunity to constrain the size evolution of luminous galaxies to $z \sim 10$, for the first time, and also pursue an exploration of the relation between size and luminosity or mass relation at $z \sim 9$–10. Previously studied $z \sim 9$–10 samples (Ono et al. 2013) consisted almost entirely of extremely faint sources with smaller, more uncertain sizes, making it difficult to optimally constrain the size evolution to $z = 9$–10 galaxies.

The purpose of this paper is to (1) measure the sizes of the candidate $z = 9$–10 galaxies reported in Oesch et al. (2014) to test if these sources are consistent with corresponding to star-forming galaxies at $z \sim 9$–10, (2) characterize the size evolution of luminous galaxies to the highest-accessible redshifts, and (3) explore any change in their star formation rate (SFR) surface density of galaxies from the earliest accessible epoch. A measurement of the size distribution of $z \sim 10$ galaxies is critical for design of current and future observations with the *James Webb Space Telescope* (*JWST*), Atacama Large Millimeter Array (ALMA), and the Extremely Large Telescopes (ELTs). We adopt $\Omega_M = 0.3$, $\Omega_\Lambda = 0.7$, $H_0 = 70$ km s$^{-1}$ Mpc$^{-1}$, consistent with recent WMAP9 (Hinshaw et al. 2013) or Planck results (Planck Collaboration et al. 2014). We express galaxy UV luminosities in units of the characteristic luminosity ($L^*_{z=3}$) at $z \sim 3$, i.e., $M_{1600}(z = 3) = -21.07$ (Steidel et al. 1999).

## 2. OBSERVATIONAL DATA

To measure the sizes, we use the public data from the XDF (Illingworth et al. 2013) and CANDELS (Grogin et al. 2011; Koekemoer et al. 2011) fields. The size measurements are

performed in the *F160W* filter drizzled images from both programs. Pixel scales are set to 0″.06 (compared to the native 0″.13 for WFC3/IR) and 5$\sigma$-limiting *F160W* magnitudes are 29.8 (XDF), 28.4 (CANDELS-deep), and 27.6 (CANDELS-wide), respectively, for a 0″.35-diameter aperture.

## 3. METHODOLOGY FOR SIZE MEASUREMENTS

A convenient and powerful tool to measure sizes accurately for faint sources is GALFIT (Peng et al. 2002, 2010). GALFIT determines the size of an object by comparing the two-dimensional profile of a galaxy with a point-spread function (PSF)-smoothed Sérsic profile and then finding the model which minimizes the value of $\chi^2$. We fix the Sérsic index to $n = 1.5$ in our fits (see Table 2, consistent with the Sérsic parameters derived for stacked $z = 4$–6 samples in Hathi et al. (2008). Fixing the Sérsic index to other values (i.e., $n = 1$–2.5) did not change the effective radius result significantly (<10%). We allow the central position to range within 3 pixels of the one determined by SEXTRACTOR (X_PEAK, Y_PEAK). In the case of a single object (XDFyj-40248004), the center was fixed to the SEXTRACTOR value. We use SEXTRACTOR to estimate the local background (128 pixels aperture) and the drizzle weight map for an estimate of noise for both the application of SEXTRACTOR and GALFIT. The sextractor run on the field yields an initial guess of the position angle and effective radius for GALFIT (see Table 2). We fix the axes ratio ($q = 1$) as these objects are mostly circular. We did try fits with GALFIT with the axes ratio ($q$) as a free parameter but the resulting axes ratio was too uncertain to be informative.

While our CANDELS and XDF reductions are already globally background-subtracted, we estimate the local background surrounding the fit objects again with GALFIT to ensure that local variations do not influence the fit results.

The dominant uncertainties in the measured sizes are the estimated background, the precise shape of the PSF, and the pixels included in the fit. For an in-depth discussion on the uncertainties and biases in size measurements with GALFIT we refer to Ono et al. (2013).

We use repeat fits of each object to estimate variance due to different PSF models. These models are from the 3D-*HST* project (v3.0 Brammer et al. 2012; van Dokkum et al. 2013; Skelton et al. 2014, http://3dhst.research.yale.edu) each derived for a specific CANDELS field, resulting in unique outer structure, and an additional *HST* PSF with forced circular symmetry. Similar to van der Wel et al. (2014), we find that the choice of PSF model only has a minor impact on the effective radius measurement, i.e., fit-to-fit variance is much lower than the error.

An important input value for GALFIT is the list of pixels to include in the shape fit. One can use either those pixels attributed to an object by SEXTRACTOR (segmentation map), all pixels in an image *except* those assigned to other objects (masked) or simply all the pixels in a cut-out area. This latter option is preferred for faint and isolated sources to minimize bias and we opt for this as the fitted sources are generally isolated from neighboring objects (Figure 2). In the case of GN-z10-1 and to a lesser degree GS-z10-1 and XDFyj-40248004, there are other sources in the GALFIT stamp. However, we found that our fit results did not improve appreciably when masking neighboring objects. We found that it was sufficient to limit the central pixel position so that it was close to the one found by SEXTRACTOR.
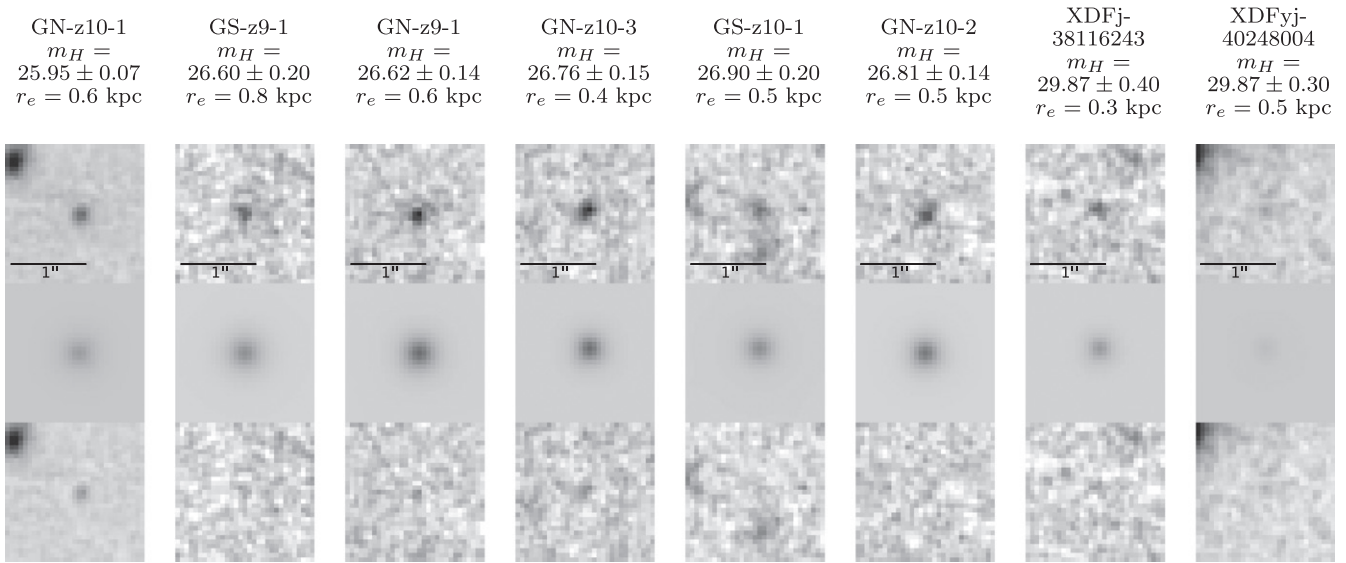
**Figure 2.** Object $F160W$ cutouts (top row), galfit models (middle row) and residual image (bottom row) for the eight $z \sim 9$–10 candidate galaxies we consider here, ranked by apparent luminosity from bright to faint (Table 1, Figure 1). Grayscale is $-2\sigma$ to $7\sigma$ centered on the background level and the scale-bar is $1''$. The six leftmost objects are the bright candidates identified by Oesch et al. (2014) in the GOODS North (GN) and GOODS South (GS) CANDELS fields, with the faint candidates identified in the XDF on the right.

**Table 1**
The $z \sim 9$–10 Candidates from the XDF and CANDELS Fields from Oesch et al. (2014) and Bouwens et al. (2014)

| Object ID | R.A. (J2000) | decl. (J2000) | $H_{160}$ | $z_{phot}$ (b) | $r_e$ (kpc)[c,d] | S/N (e) | $\log_{10}(M^*)$ $(M_\odot)$[f] | $L/L^*_{z=3}$ | $\chi^2$ | References |
|---|---|---|---|---|---|---|---|---|---|---|
| GN-z10-1 | 12:36:25.45 | +62:14:31.6 | $25.95 \pm 0.07$ | $10.2 \pm 0.4$ | $0.6 \pm 0.3$ | 18.1 | 9.36 | 1.57 | 18.70 | (1), (2) |
| GS-z9-1 | 03:32:32.05 | −27:50:41.7 | $26.60 \pm 0.20$ | $9.3 \pm 0.5$ | $0.8 \pm 0.2^g$ | 5.7 | 9.17 | 0.76 | 1.21 | (1) |
| GN-z9-1 | 12:36:52.24 | +62:18:42.7 | $26.62 \pm 0.14$ | $9.2 \pm 0.3$ | $0.6 \pm 0.1$ | 9.0 | 9.20 | 0.73 | 1.28 | (1) |
| GN-z10-3 | 12:36:04.08 | +62:14:29.9 | $26.76 \pm 0.15$ | $9.5 \pm 0.4$ | $0.4 \pm 0.1^a$ | 9.0 | 9.17 | 0.67 | 1.38 | (1), (2) |
| GS-z10-1 | 03:32:26.97 | −27:46:28.3 | $26.90 \pm 0.20$ | $9.9 \pm 0.5$ | $0.5 \pm 0.1$ | 7.2 | 9.10 | 0.63 | 2.00 | (1), (2) |
| GN-z10-2 | 12:37:22.73 | +62:14:22.7 | $26.81 \pm 0.14$ | $9.9 \pm 0.3$ | $0.5 \pm 0.1$ | 7.8 | 9.15 | 0.68 | 1.34 | (1), (2) |
| XDFj-38116243 | 03:32:38.11 | −27:46:24.3 | $29.87 \pm 0.40$ | $9.9^{+0.7}_{-0.6}$ | $0.3 \pm 0.1^a$ | 4.7 | 8.06 | 0.04 | 1.48 | (2), (3), (4) |
| XDFyj-40248004 | 03:32:40.23 | −27:48:00.3 | $29.87 \pm 0.30$ | $8.9^{+0.6}_{-0.3}$ | $0.5 \pm 0.9$ | 4.3 | 7.63 | 0.04 | 5.38 | (2), (3) |

**Notes.**

[a] Indicates a marginally resolved source.

[b] Photometric redshifts from Oesch et al. (2014) for the GN sources (their Table 2) and Bouwens et al. (2014), using the ZEBRA photometric redshift code (Feldmann et al. 2011) in both cases.

[c] Median uncertainty in these $r_e$ values is 0.2 kpc.

[d] This is the major axis size reported by GALFIT with the axis ratio fixed such that $q = 1$; equivalent to the circularized radii $r = \sqrt{q} \times r_e$ found elsewhere.

[e] The signal-to-noise calculated from the light enclosed in a $0''36$-diameter aperture (see Bouwens et al. 2014), conform with the estimate from Oesch et al. (2013b, 2014).

[f] Mass estimates are from Oesch et al. (2014) (their Table 6). Mass estimates for $z \sim 9$–10 candidates from the XDF data assume the same mean $M/L_{F160W}$ ratio, i.e., $0.32\ M_\odot/L_\odot$ as Oesch et al. (2014) found for their bright sources.

[g] Galfit parameters for GS-z9-1 are available from the CANDLES team (van der Wel et al. 2012, 2014, http://www.mpia-hd.mpg.de/homes/vdwel/candels.html), which lists: $m = 27.1 \pm 0.3$, $r_e = 0''05 \pm 0.03$ (corresponding to 0.2 kpc) and $n = 2.83 \pm 2.81$ (flag = 2, S/N = 6.1). The difference in $r_e$ can be attributed to van der Wel et al. (2014)'s leaving the Sérsic index free and differences in our segmentation maps for the source. For more details, see Section 4.1. While van der Wel et al. (2014) find a smaller size for this source, overall our size measurements agree quite well (within $\sim 20\%$) with those from van der Wel et al. (2014) and Grazian et al. (2012).

**References.** (1) Oesch et al. (2014), (2) Bouwens et al. (2014), (3) Oesch et al. (2013a), (4) Bouwens et al. (2011a).

## 4. RESULTS

Here we measure sizes for the six particularly bright $z \sim$ 9–10 candidates discovered by Oesch et al. (2014) in CANDELS and two faint candidates identified by Oesch et al. (2013a) and Bouwens et al. (2014) from the XDF. The bright $z \sim$ 9–10 candidates were identified using a $J - H > 0.5$, $H - [4.5] < 2$, and optical+Y-non-detection criterion, while the faint $z \sim 10$ candidates were identified with

$J - H > 1.2$, $H - [3.6] < 1.4$, and optical+Y-non-detection criterion.

Figure 2 shows the $F160W$ data, our GALFIT model and the residual image for two $z \sim 9$–10 candidate galaxies. The reported values are the $R_e$ value from galfit, i.e., the effective radius along the major axis but with the axes ratio ($q$) fixed to unity and therefore identical to the "circularized" radius ($\sqrt{q} \times R_e$). Typical half-light radii are between $0''10$ and
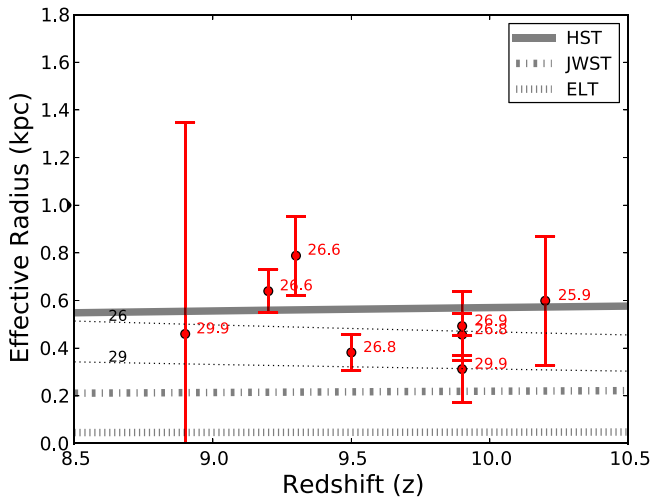
**Figure 3.** Expected size–redshift relation from the simple model of Wyithe & Loeb (2011) (Equation (4)), the nominal diffraction limits for *HST*/WFC3, *JWST* and a 30 m ELT (Equation (5)) and our size measurements at their photometric redshifts with their apparent AB magnitude (red text). The thin dotted lines are based on the Wyithe & Loeb (2011) model for galaxy sizes (Equation (4)) with an $\alpha = -2.27$ slope for the luminosity function. This value is the determination from Bouwens et al. (2014) for the $z \sim 10$ population. The agreement between the data and the model anchored on earlier observations illustrates that while a simple model suffices to predict sizes, it needs to be anchored to high-redshift measurements if one is to plan observations of these earliest epochs of galaxy evolution with future observatories such as *JWST* and ELT.

$0\rlap{.}''25$, corresponding to $\sim 0.5$ kpc at their respective redshifts (Table 1). The mean uncertainty in effective radius is $0\rlap{.}''06$ (0.28 kpc). Fits to these faint objects are reasonably good (reduced $\chi^2 \sim 1$–19). Table 1 lists the $H_{160}$ apparent magnitude determined with GALFIT and the luminosity and inferred stellar mass from that value.

Ryan et al. (2011) and Holwerda et al. (2014) explore the SEXTRACTOR effective radius ($r_e$) of known Galactic stars in CANDELS. They consider sources with $r_e < 0\rlap{.}''15$ (uncorrected for the PSF) to be unresolved ($0\rlap{.}''1$ corrected for the *F125W* PSF). In the case of GALFIT, the minimum effective radius can be smaller because the model is convolved with the PSF. Figure 3 illustrates how the majority of our sources are indeed resolved with *HST*.

Two of the candidate high-redshift galaxies have GALFIT effective radii indicating they are marginally resolved sources ($r_e < 0\rlap{.}''1$), one from CANDELS (GN-z10-3) and one in the XDF (XDFj-38116243). The CANDELS sample is therefore better resolved compared to the XDF sources: 50% compared to 17%. The mean effective radii are $\langle r_e \rangle = 0\rlap{.}''09$ (XDF) and $\langle r_e \rangle = 0\rlap{.}''13$ (CANDELS), respectively, illustrating the benefits of the latter sample.

### 4.1. Comparison to Previous Results

As a check on the GALFIT sizes, we measure the sizes for $z \sim 7$ galaxy candidates from the CANDELS South (Bouwens et al. 2014) in the same manner as the $z \sim 9$–10 candidates and compare these to the results from van der Wel et al. (2014). Both size measurements were obtained from the CANDELS *F160W* mosaics. We note however, that we made use of the reductions from the 3D-*HST* team (Skelton et al. 2014) and an rms map based on the drizzle weight map (see Casertano et al. 2000; Holwerda 2005). We find good agreement in the

mean between the GALFIT radii we measure and the size measurements in the van der Wel et al. (2014) catalog (within 14% for 29 sources). We note that van der Wel et al. (2014) leave the Sérsic index as a free parameter, ranging up to $n = 3$, whereas we keep it fixed ($n = 1.5$). Refitting the same 29 $z \sim 7$ sources with the van der Wel et al. (2014) reported Sérsic indices ($n$), we arrive at similar sizes ($< 0\rlap{.}''05$ difference).

A second check is provided by the $z \sim 7$ SEXTRACTOR catalog from Grazian et al. (2012), and assuming exponential disks at this redshift. Matching this catalog against our $z \sim 7$ catalog, we find reasonable agreement between the measured sizes (within $\lesssim 20\%$) for the eight galaxies present in both samples.

### 4.2. Confirmation of Oesch et al. (2014) Photometric $z \sim 9$–10 Selection

It is useful to compare the sizes we measure for the bright $z \sim 9$–10 candidates from Oesch et al. (2014) with that expected extrapolating the sizes of lower-redshift galaxies to $z \sim 10$ to see if the candidates seem consistent with lying at $z \sim 10$ as the strong photometric evidence would suggest. The mean effective radius for both bright and faint sources ($\langle r_e \rangle = 0.5$ and 0.4 kpc, respectively) conforms to general expectations for star-forming galaxies at $z \sim 9$–10 (see Section 4.6). For comparison, we also measure GALFIT sizes for six potential interlopers to the Oesch et al. (2014) selection, i.e., satisfying all the $z \sim 9$–10 criteria except that their $H - [3.6]$ or $H - [4.5]$ color is very red. These low-redshift and likely dusty interlopers have a mean effective radius of $\langle r_e \rangle = 0\rlap{.}''59$, substantially larger than the $\langle r_e \rangle \sim 0\rlap{.}''13$ radius we find for our bright $z \sim 9$–10 sample.

In spite of the encouraging results from this test, we emphasize that the strongest constraints on the high-redshift nature of these sources come from the accurate photometric observations available for each of these sources, which combined strongly favor a $z \sim 9$–10 identification. Nevertheless, this size test does provide evidence that the Oesch et al. (2014) candidate $z = 9$–10 galaxies do not correspond to some exotic (yet unseen) population of contaminants, as appears to have occurred when an unprecedented extreme emission-line galaxy (EELG) contaminated the Bouwens et al. (2011a) $z = 10$ photometric selection.

More generally, we have found a general correlation between the measured size of sources with *HST* photometry consistent with their corresponding to $z \sim 9$–10 galaxies and their $H - \mathrm{IRAC}$ colors. As shown in Figure 4, the measured sizes of Oesch et al. (2014) candidates are all smaller than any of the IRAC-red interlopers to the Oesch et al. (2014) selection. We note that the IRAC-red interlopers are about equally numerous as sources in our $z \sim 9$–10 sample. Without information from deep *Spitzer*/IRAC imaging on these sources, they could constitute a serious contamination of any $z > 9$ sample. Size could therefore serve as a proxy for IRAC color information, where the latter is lacking. The separation in both $H - [3.6]$ color and size in Figure 4 adds confidence that our candidate $z \sim 9$–10 galaxies are indeed at these redshifts.

### 4.3. Size–Luminosity Relation

The observed correlation between the physical sizes of galaxies and their luminosities provides us with information on how the physical scale of star-forming regions in galaxies scales with the SFR across cosmic time. Figure 5 shows the
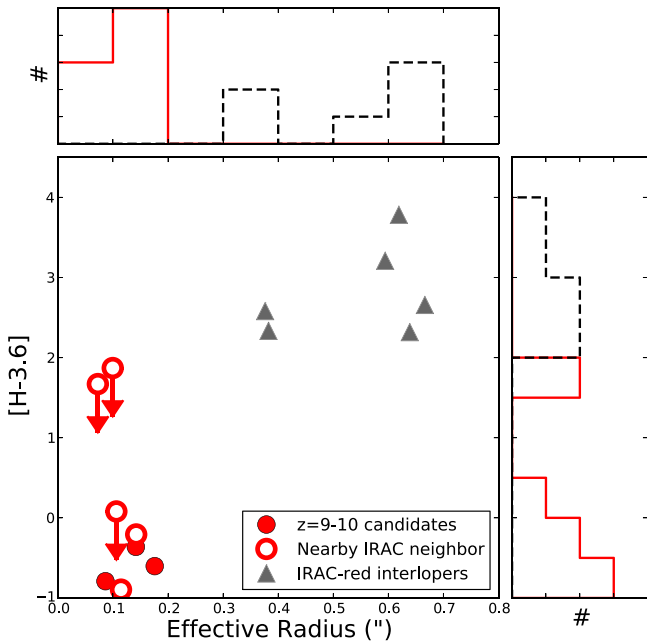
**Figure 4.** $z \sim 9$–10 galaxy candidates from Oesch et al. (2013b, 2014) and the interlopers to the $z \sim 9$–10 selection where the $H - [3.6]$ or $H - [4.5]$ criterion is not applied. Those objects with close companions in the IRAC 3.6 $\mu$m images (see Figure 4 in Oesch et al. 2013b and Figure 2 in Oesch et al. 2014) are indicated with open circles and with arrows where lower limits on the flux measurements are relevant. The effective radii ($r_{\rm e}$) and $H - 3.6$ colors for $z \sim 9$–10 galaxy candidates from Oesch et al. (2014, red circles) and interlopers to a $z \sim 9$–10 selection (gray triangles) when no $H - [3.6]$ or $H - [4.5]$ criterion is applied. The $z \sim 9$–10 galaxies and the lower-redshift interlopers separate well in both their measured $H - [3.6]$ colors and sizes. This suggests that the sizes of $z \sim 9$–10 candidates could serve as an alternate constraint on the high-redshift nature of $z \sim 9$–10 candidates where no *Spitzer*/IRAC data are available (e.g., as with the BORG program).
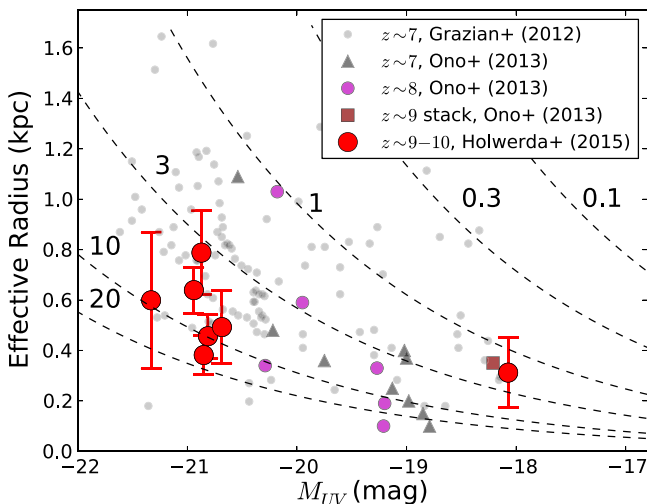


**Figure 5.** Observed UV luminosities (1450 Å at $z = 10$) vs. effective radius for our sample of $z \sim 9$–10 candidate galaxies (excluding the galaxy with the most uncertain size, XDFyj-40248004). Light gray points are the sizes and absolute luminosities in *F160W* from Grazian et al. (2012, PSF-corrected), for their $z \sim 7$ sample, while the dark gray, magenta and brown points are the $z \sim 7$, $z \sim 8$, and $z \sim 9$–10 samples respectively, from Ono et al. (2013). The red dotted line and shaded area are the best fit and $1\sigma$ uncertainty on the luminosity–size relation for our sources. The dashed lines are star formation surface density levels of $\Sigma_{\rm SFR} = 0.1, 0.3, 1, 3, 10, 20 \, M_{\odot} \, {\rm yr}^{-1} \, {\rm kpc}^{-2}$ (assuming no dust or emission lines in the rest-frame UV).

relationship between the UV luminosity and the effective radius for our $z = 9$–10 sample, with the exception of one source from our faint sample XDFyj-40248004 which is not shown, since its size measurement is quite uncertain (Table 1). For comparison, we also include the sizes from Grazian et al. (2012) and Ono et al. (2013) in this figure. The caveats are that (1) UV is sensitive to longer-duration star formation, (2) the conversion from UV luminosity to SFR for low-metallicity, high-mass stars is uncertain, and (3) a lack of emission line observations, which track more stochastic star formation. Our candidate $z \sim 9$–10 galaxies have a similar range of sizes and luminosities as the $z \sim 7-8$ galaxies from Grazian et al. (2012) and Ono et al. (2013).

To help interpret the relationship between size and luminosity, it is useful to fit a linear relation to the points in Figure 5:

$$R = R_{*} \left( \frac{L}{L_{*}(z = 3)} \right)^{b} \tag{1}$$

similar to the treatment at lower redshifts (Huang et al. 2013). The slopes ($b$) we find for the $z = 9$–10 sample, those from Huang et al. (2013), and the ones we derive for the Mosleh et al. (2012) and Ono et al. (2013) samples are presented in Table 3. The slopes of the luminosity–size relation for Ono et al. (2013) and this work are very uncertain due to the small number of sources in the present samples, but are plausibly consistent with what has been found at lower redshifts. All values of the luminosity–slope relation are consistent with a $b \sim 0.25$ slope for the entire redshift range.

The outstanding issue with the $z \sim 9$–10 size–luminosity relation is that the statistical weight for the fit of the slope hinges on a single point (XDFj-38116243). However, we note that the stacked $z \sim 9$–10 result from Ono et al. (2013) is near this point as well. Not only will a large sample size improve the determination of the relation, preferably, it will need to be distributed over more than a magnitude of luminosity (Figure 5), as well as include a correction for strong emission lines.

### 4.4. Star Formation Rate Surface Density

The sizes and absolute luminosity in the rest-frame ultra-violet are intimately linked to the SFR density in these systems, informing us of the conditions in these first stellar systems. The SFR surface density can be tied to the absolute UV magnitude and effective radius by

$$\begin{aligned} M_{\rm UV} = &-2.5 \\ &\times \log_{10} \left( \frac{\Sigma_{\rm SFR} \times r_{\rm e}^2}{10[{\rm pc \ in \ cm}]^2 \times 2.8 \times 10^{-28}} \right) - 48.6 \end{aligned} \tag{2}$$

from Ono et al. (2013), where $\Sigma_{\rm SFR}$ is in $M_{\odot} \, {\rm yr}^{-1} \, {\rm kpc}^{-2}$ and $r_{\rm e}$ in kiloparsecs. Neither dust extinction or strong emission lines are assumed in this conversion.

Figure 5 shows the relation between our effective radii and the implied absolute magnitudes for different values of the star formation rate surface density. Galaxies in our sample are consistent with $\Sigma_{\rm SFR} \sim 1$–$20 \, M_{\odot} \, {\rm yr}^{-1} \, {\rm kpc}^{-2}$. Ono et al. (2013) found similar SFR surface densities for $z \sim 7-8$

**Table 2**
Galfit Settings and Parameters

| Order | Default, Example or Script Variable | Galfit Description |
|---|---|---|
| A) | GOODS-S_F160W_stamp.fits | Input data image (FITS file) |
| B) | object_name_model.fits | Output data image block |
| C) | rms.fits | Sigma image name (made from data if blank or "none") |
| D) | GOODS-S_F160W_psf.fits | Input PSF image and (optional) diffusion kernel |
| E) | 1 | PSF fine sampling factor relative to data |
| F) | seg.fits | Bad pixel mask (FITS image or ASCII coord list) |
| G) | None | File with parameter constraints (ASCII file) |
| H) | $x_c$(se)-50 $x_c$(se)+50 $y_c$(se)-50 $y_c$(se)+50 | Image region to fit (xmin xmax ymin ymax) |
| I) | 180 180 | Size of the convolution box (x y) |
| J) | 25.9463 | Magnitude photometric zeropoint |
| K) | 0.060 0.060 | Plate scale (dx dy) [arcsec per pixel] |
| O) | Regular | Display type (regular, curses, both) |
| P) | 0 | Choose: 0 = optimize, 1 = model, 2 = imgblock, 3 = subcomps |
| 0) | Sersic | Component type |
| 1) | $x_c$(se) $y_c$(se) 1 1 | Position x, y |
| 3) | $m_{160}$(se) 1 | Integrated magnitude |
| 4) | $r_e$(se) 1 | $R_e$ (effective radius) [pix] |
| 5) | 1.5000 0 | Sérsic index n (de Vaucouleurs n = 4) |
| 6) | 0.0000 0 | … |
| 7) | 0.0000 0 | … |
| 8) | 0.0000 0 | … |
| 9) | 1.0 0 | Axis ratio (b/a) |
| 10) | PA(se) 1 | Position angle (PA) [deg: Up = 0, Left = 90] |
| Z) | 0 | Skip this model in output image? (yes = 1, no = 0) |

**Note.** Parameters marked with (se) are script variables for which we used the SEXTRACTOR values.

**Table 3**
The Slopes of the Luminosity–Size Relation (Top Ones from the Summary in Huang et al. 2013)

| Redshift (z) | Intercept ($R_*$, kpc) | Slope (b) | Reference |
|---|---|---|---|
| 0 | 5.93 ± 0.28 | 0.21 ± 0.03 | (1) |
| 0 | 3.47 | 0.26 | (2) |
| 0 | … | 0.32 ± 0.01 | (3) |
| 4 | $1.34^{+0.10}_{-0.11}$ | 0.22 ± 0.06 | (4) |
| 5 | $1.19^{+0.21}_{-0.16}$ | 0.25 ± 0.15 | (4) |
| 7 | 0.86 ± 0.04 | 0.24 ± 0.06 | (5) |
| 7 | 1.55 ± 0.31 | 1.05 ± 0.21 | (6) |
| 8 | 1.44 ± 1.07 | 1.03 ± 0.75 | (6) |
| 9–10 | 0.57 ± 0.06 | 0.12 ± 0.09 | This work |

**Note.** The slopes for the Mosleh et al. (2012), Grazian et al. (2012), and Ono et al. (2013) samples were derived by us based on the published values.
**References.** (1) de Jong & Lacey (2000), (2) Shen et al. (2003), (3) Courteau et al. (2007), (4) Huang et al. (2013), (5) derived by us from the Grazian et al. (2012) data, (6) derived by us from the Ono et al. (2013) data.

galaxies, and Oesch et al. (2010) and Shibuya et al. (2015) show there is limited evolution in the average SFR surface density (for $>0.3L^*_{z=3}$ galaxies) from $z \sim 4$ to 8 with their mean bracketed by our values.

### 4.5. Mass–Size Relation

The availability of size measurements and mass estimates for our sources allows us to examine the mass–size relation to $z \sim 9$–10. Our mass estimates for the bright sources are from Oesch et al. (2014) and for the HUDF/XDF sources from the $H_{F160W}$

using the mean M/L ratio of the Oesch et al. (2014) values ($0.36\ M_\odot/L_\odot$). We caution that there are large potential systematic uncertainties in these estimates, due to the likely presence of nebular emission lines of unknown strength in the IRAC fluxes (rest-frame optical) which Oesch et al. (2014) use to derive the masses for their $z \sim 9$–10 sample.

Figure 6 shows the relation between mass and size with comparison samples at high-redshift $z = 2$, 6, and 7 (van der Wel et al. 2014; Mosleh et al. 2012; Grazian et al. 2012; Ono et al. 2013, respectively) and the local relations from SDSS (Shen et al. 2003) and GAMA (Baldry et al. 2012). There is only a very weak mass–size relation compared to the steeper relation at $z = 0$ (Shen et al. 2003; Baldry et al. 2012) or $z = 2$ (van der Wel et al. 2014). Our $z = 9$–10 sample occupies the same mass–size space as the $z = 6$ sample from Mosleh et al. (2012). Converted to mass following the Stark et al. (2013) prescription, the $z \sim 7$ samples from Grazian et al. (2012) and Ono et al. (2013) have sizes similar to the most massive galaxies from our $z = 9$–10 sample, but with a few outliers to $r_e \sim 1.5$ kpc. Overall, we find much weaker evolution in the mass–size relation than in the luminosity–size relation. This is not especially surprising given the evolution in the sSFRs (and hence mass-to-light ratio (M/L) ratios) of galaxies from $z \sim 7$ to $z \sim 3$ (Stark et al. 2013; González et al. 2014). The M/L ratio evolution largely cancels evolution in the sizes of galaxies at fixed luminosity, resulting in only a weakly evolving size–mass relation.

To quantify the relation between size and mass, we fit a linear relation to the points in Figure 6:

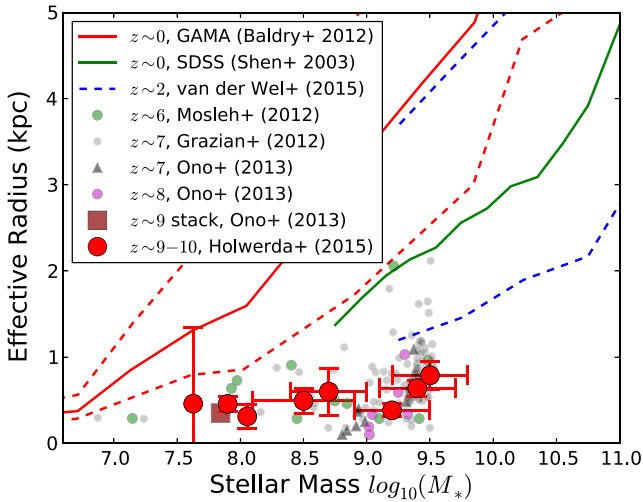$$R = R_0 \left( \frac{M_*}{M_0} \right)^{\beta} \qquad (3)$$

**Figure 6.** Mass–size relationship for our sample of $z \sim 9$–$10$ galaxies from CANDELS and the XDF. For comparison, we show the $z \sim 2$ (blue dashed interval, van der Wel et al. 2014), the $z \sim 6$ (green points Mosleh et al. 2012), the $z \sim 7$ and $z \sim 8$ galaxies based on the (Grazian et al. 2012, light gray and Ono et al. 2013, dark gray and magenta respectively) catalogs (corrected for emission line contamination and adopting a *M/L* ratio from Stark et al. 2013, for the latter two respectively). The dark red square is the single $z \sim 9$–$10$ stacked size measurement from Ono et al. (2013), similarly converted. The mass–size relations for $z = 0$ blue galaxies are from GAMA (red line, Baldry et al. 2012) and SDSS (green line, Shen et al. 2003). The thick red dotted line and shaded area are our best fit to the $z \sim 9$–$10$ data with $1\sigma$ uncertainty.

where we fix $M_0 = 1.0 \times 10^9 M_\odot$ since it corresponds to approximately the median stellar mass of our sample.

The intercept ($R_0$ at $M_0$) and slopes ($\beta$) we find are listed in Table 4 and plotted as a function of redshift in Figure 7. In general, these slopes are uncertain but comparable with those found for earlier epochs for the luminosity–size relation (of star-forming galaxies), which can be expected if the mass-to-light ratio conversion is not mass-dependent over the range probed. We note that the $z \sim 7$ relations based on the Mosleh et al. (2012) and Ono et al. (2013) samples are poorly constrained. From theory, the relation between luminosity or stellar mass with size is expected to be slightly shallower than $\beta \sim 1/3$ (see e.g., Dutton & van den Bosch 2012; Stringer et al. 2014).

The slope is typically around 0.25 for most star-forming, late-type galaxies over the age of the universe (see van der Wel et al. 2014 for mass–size relations, Figure 7 and Table 4). The value we find for the $z = 9$–$10$ sample is somewhat flatter (Figure 7), but this result is not especially significant and may change as more $z \sim 9$–$10$ galaxies are identified and characterized. We have already noted that the derivation of stellar mass for current $z \sim 9$–$10$ candidates is quite uncertain due to a number of issues (dust extinction, nebular lines of unknown strength). However, we would expect the slopes we derive to be very similar however we deal with these uncertainties. The lack of a slope may be indicative that these galaxies are indeed the very first ones to be formed and are not yet completely virialized (see Section 2 from Stringer et al. 2014). In this case, the over-dense regions have collapsed—the lowest density ones first—already forming the galactic system but without sufficient dynamical time for the system to reach equilibrium and hence virial relations between mass and size. The different collapse times for different halo sizes also mean that the mass–size relation is not what is expected even for

**Table 4**
The Slopes of the Mass–Size Relation

| Redshift ($z$) | Intercept ($R_0$, kpc) | Slope ($\beta$) | Reference |
|---|---|---|---|
| 0.25 | $2.72 \pm 0.04$ | $0.25 \pm 0.02$ | (1) |
| 0.75 | $2.55 \pm 0.04$ | $0.22 \pm 0.01$ | (1) |
| 1.25 | $2.12 \pm 0.04$ | $0.22 \pm 0.01$ | (1) |
| 1.75 | $1.82 \pm 0.04$ | $0.23 \pm 0.01$ | (1) |
| 2.25 | $1.50 \pm 0.04$ | $0.22 \pm 0.01$ | (1) |
| 2.75 | $1.60 \pm 0.04$ | $0.18 \pm 0.02$ | (1) |
| 6 | $0.75 \pm 0.18$ | $0.14 \pm 0.20$ | (2) |
| 7 | $0.64 \pm 0.05$ | $0.24 \pm 0.08$ | (3) |
| 7 | $0.27 \pm 0.07$ | $1.35 \pm 0.34$ | (4) |
| 9–10 | $0.57 \pm 0.05$ | $0.12 \pm 0.06$ | This work |

**Note.** The lower-redshift values are from van der Wel et al. (2014) values, derived for the late-type star-forming galaxies in their sample. The slopes for the Mosleh et al. (2012), Grazian et al. (2012) and Ono et al. (2013) samples were derived by us based on the derived masses (using the Stark et al. 2013, conversions), without assuming any evolution in the nebular emission EWs. The intercept ($R_0$) is fixed at a mass of $1.0 \times 10^9 M_\odot$.
**References.** (1) van der Wel et al. (2014), (2) derived by us from the Mosleh et al. (2012) data, (3) derived by us from the Grazian et al. (2012) data, (4) derived by us from the Ono et al. (2013) data.
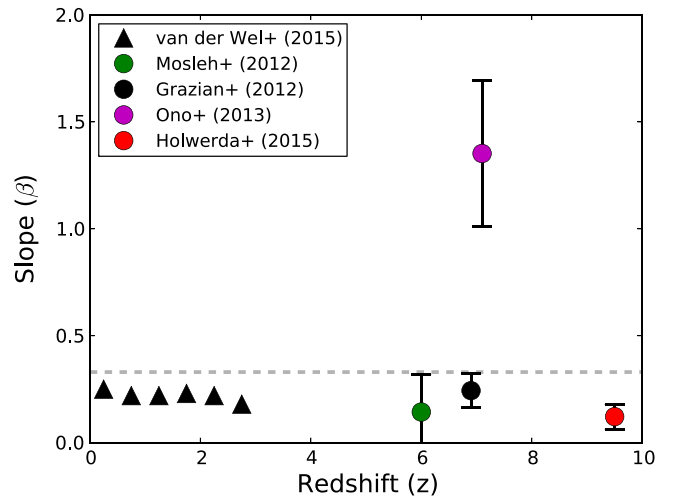


**Figure 7.** Slope of the stellar mass–size relation ($\beta$) as a function of redshift. The lower-redshift points are from van der Wel et al. (2014), derived from their fit. Redshift $z \sim 6$–$7$ points are our fits based on the inferred mass–size relations derived from Mosleh et al. (2012), Grazian et al. (2012) and Ono et al. (2013), with mass-to-light corrections from Stark et al. (2013). The dashed line is the maximum ($\beta \simeq 1/3$). The $z \sim 9$–$10$ sample exhibits a practically flat slope compared to most previous work.

recently virialized systems. We reiterate, however, that the sample is small and the slope still uncertain. A larger $z \sim 9$–$10$ sample would be needed to accurately determine this relation.

### 4.6. Redshift–Size Relationship

The discovery of a sample of luminous sources at $z \sim 9$–$10$ provides us with additional leverage to constrain the size evolution of star-forming galaxies to $z \sim 10$. Figure 8 shows the evolution of mean effective radius with redshift for luminous ($>0.3L^*_{z=3}$) and lower-luminosity ($<0.3L^*_{z=3}$) galaxies. It is important to be mindful of luminosity limits across redshift in examining size–redshift evolution (see e.g., Cameron & Driver 2007). For comparison, we include the
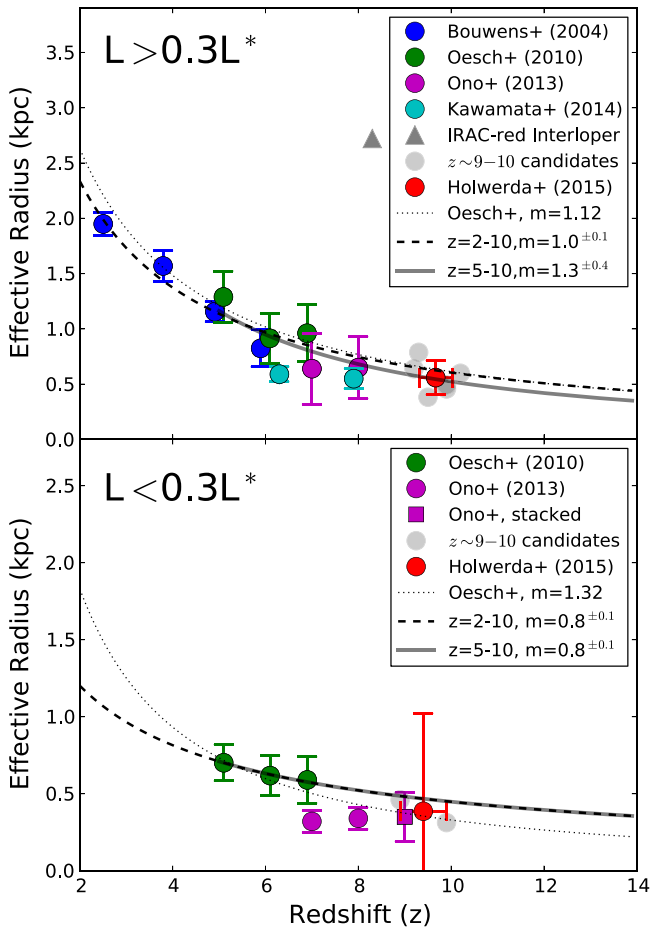
**Figure 8.** The effective radius as a function of redshift for our sample for both bright ($L > 0.3L_{z=3}^*$, top panel) and lower-luminosity galaxies ($L < 0.3L_{z=3}^*$, bottom panel). For comparison, we show the mean sizes from earlier epochs from Bouwens et al. (2004), Oesch et al. (2010), Ono et al. (2013), and Kawamata et al. (2014). The mean size of the six potential interlopers to a $z \sim 9$–10 selection (see Section 4.1) is well above any expected relation at $z \sim 9$. We do not include the Bouwens et al. (2011a) $z \sim 2/z \sim 12$ candidate as there is considerable doubt as to whether it is at $z \sim 12$ (Bouwens et al. 2013; Brammer et al. 2013; Capak et al. 2013; Ellis et al. 2013; Pirzkal et al. 2013). The dotted line shows the best fits from Oesch et al. (2010). The dashed lines are our fits to the Bouwens et al. (2004) and Oesch et al. (2010) values combined with our mean size constraints at $z \sim 9$–10. We exclude the Ono et al. (2013), and Kawamata et al. (2014) points because these were derived using different methods. The solid gray line the best fit for the high redshift ($z > 5$) points alone. The mean size of $L > 0.3L_{z=3}^*$ galaxies scale as $(1 + z)^{-1}$.

mean size measurements from Bouwens et al. (2004), Oesch et al. (2010), Ono et al. (2013), and Kawamata et al. (2014). We refer the reader to Shibuya et al. (2015) for a discussion on the size evolution using parametrizations other than the mean (e.g., mode).

As the best-fit trend may be partially driven by the small uncertainties on the lower-redshift points, the value of our new $z \sim 9$–10 size measurements for constraining the size evolution is somewhat limited assuming a fixed size–redshift scaling. Including our new $z \sim 9$–10 size measurements and assuming a $(1 + z)^{-m}$ scaling of size with redshift, the best-fit size–redshift scaling $m$ we find is $1.04 \pm 0.09$. Rederiving the scaling without our new constraints at $z \sim 9$–10, we find $1.01 \pm 0.10$. Previously, Bouwens et al. (2004, 2006) and Oesch et al. (2010) found a very similar dependence of mean size on redshift (see also Shibuya et al. 2015). For lower-luminosity ($<0.3L_{z=3}^*$) galaxies, the evolution is much less certain

**Table 5**
The Best-fit Parameters, Intercept and Slope, for the Luminous and Lower-luminosity Samples Fit Over Different Redshift Ranges.

| Redshift | Intercept | Slope |
|---|---|---|
| $z$ | $R_0(z = 4)$ | $m$ |
| $L > 0.3L^*$ | | |
| 2–8 | $1.38 \pm 0.04$ | $1.01 \pm 0.10$ |
| 2–10 | $1.37 \pm 0.04$ | $1.04 \pm 0.09$ |
| 5–8 | $1.62 \pm 0.60$ | $1.64 \pm 1.17$ |
| 5–10 | $1.48 \pm 0.26$ | $1.32 \pm 0.43$ |
| $L < 0.3L^*$ | | |
| 5–8 | $0.80 \pm 0.03$ | $0.71 \pm 0.11$ |
| 5–10 | $0.81 \pm 0.03$ | $0.76 \pm 0.12$ |

**Note.** If one includes the $z \sim 9$–10 data in the high-redshift ($z > 5$) fits, the accuracy improves significantly.

($m = 0.8 \pm 0.1$), though the $(1 + z)^{-1.32}$ relation from Oesch et al. (2010) also provides a reasonable fit. Such a dependence is a generic expectation of theoretical models (e.g., Somerville et al. 2008; Wyithe & Loeb 2011; Stringer et al. 2014, and others).

While we note only marginal improvements in our determination of the best-fit scaling including our new measurement, this is in the context of a model where galaxies are assumed to scale as a power of $1 + z$ at all redshifts. It is conceivable that at early enough times galaxy sizes could scale differently (e.g., due to the impact of the UV ionizing background on gas cooling). In this context, we have provided the first published constraints on the size evolution of luminous galaxies from $z \sim 10$ to $z \sim 8$.

To illustrate, one can fit the evolution at the earliest epochs ($z \geqslant 5$), where the statistical weight is no longer in the lowest redshift points. We do so with and without our $z \sim 9$–10 constraint for both the luminous ($>0.3L^*$) and lower-luminosity samples. We plot these fits to different redshift ranges in Figure 8 and provide the best-fit parameters in Table 5. Because so much weight is in the lower redshift points ($z < 5$), the errors are obviously the smallest if one includes the full redshift range ($z = 2$–10). However, the inclusion of our latest high-redshift point improves the accuracy of the slope dramatically if one concerns oneself with the high-redshift evolution of sizes (Table 5).

While the present study confirms that source size follows an approximate $(1 + z)^{-1}$ scaling to very early times, it will be interesting to explore how the redshift-effective radius relation evolves for lower-mass galaxies as information on such systems become available in the future. For example, better relations between size and redshift, luminosity or mass will become available through expanded $z \sim 9$–10 samples based on near-infrared photometric selections similar to the CANDELS ones using the future Frontier Fields program (e.g., Kawamata et al. 2014), an extension to $z \sim 9$–10 for the BoRG program (Trenti 2014) and in the very long term with the *EUCLID* (Laureijs et al. 2011) or *WFIRST* (Spergel et al. 2013) satellites.

## 5. DISCUSSION

In this paper we take advantage of six new bright $z \sim 9$–10 candidate galaxies within CANDELS (Oesch et al. 2014) and

their size information (1) to test their plausibility as $z \sim 9$–10 sources and (2) to extend the study of the size–luminosity and size–mass relationship to $z \sim 10$.

While most redshift $z \sim 9$–10 candidate galaxies are unambiguously resolved ($r_e > 0\farcs1$) with *HST* CANDELS or XDF *F*160*W* data (Figure 2), the brighter sources in our $z \sim 9$–10 CANDELS sample are larger ($\langle r_e \rangle = 0\farcs13$) and better resolved than the fainter $z \sim 10$ candidates in the HUDF/XDF ($<r_e> = 0\farcs09$), allowing for a more optimal constraints on the sizes.

We find that the measured sizes can provide a useful test of the high-redshift nature of $z \sim 9$–10 selections. In particular, we find excellent agreement between the sizes of our candidates and the extrapolation from lower redshift; interlopers to $z \sim 9$–10 selections are in general $4\times$ larger (Figures 4 and 8). In the case of *HST* samples without IRAC coverage (e.g., the BORG[z9] *HST*/WFC3 pure-parallel survey), the size of the candidate high redshift galaxies can therefore potentially serve as an useful alternate constraint to select $z > 9$ candidates.

Second, we quantify the relationship between galaxy size and its luminosity at $z \sim 9$–10. The slope of the luminosity–size relation is lower than at $z = 0$–6, but our sample is small and the uncertainties large.

Third, the absolute magnitude and effective radii of the $z = 9$–10 galaxies imply a high average value of the star formation surface density ($\Sigma_{SFR} = 4\,M_{\odot}\,\mathrm{yr}^{-1}\,\mathrm{kpc}^{-2}$, Figure 5), consistent with earlier estimates at $z = 4$–8 (Oesch et al. 2010; Ono et al. 2013; Shibuya et al. 2015).

Fourth, we also explore the relationship between galaxy size and the stellar mass. The mass–size relation slope (Figure 7) for the $z \sim 9$–10 sample is uncertain but flatter than the other comparison samples or the lower-redshift values reported in van der Wel et al. (2014).

Finally, for the first time, this resolved sample allows us to extend the redshift–size relation to $z \sim 10$, confirming that $>0.3L^*_{z=3}$ galaxies follow an approximate $(1 + z)^{-1}$ scaling as early as $z = 10$.

The mean sizes of these galaxies are informative for planning future extreme high-redshift observations with facilities such as *EUCLID*, *WFIRST*, *JWST*, ALMA and the various ELTs (see Figure 3), specifically their sizes and the implied star formation surface densities.
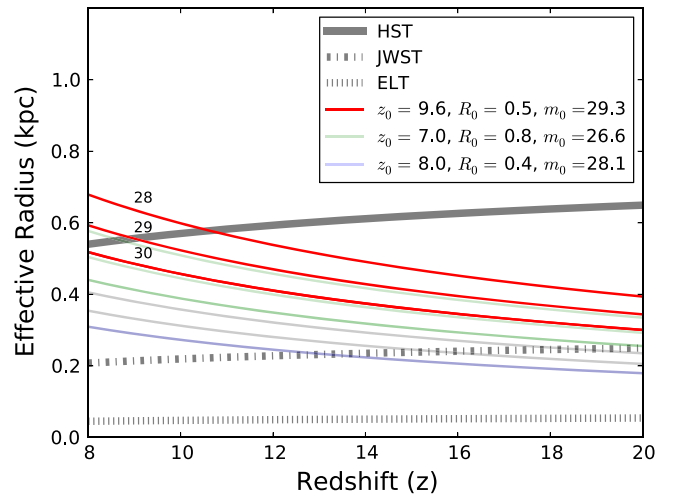
**Figure 9.** Expected size–redshift relation from the simple model of Wyithe & Loeb (2011), normalized with different size distribution observed at high redshift ($R_0$ for a $m_0$ galaxy at $z_0$). The blue and green lines are $z = 7$ and $z = 8$ normalizations based on Oesch et al. (2009) for $m_0 = 28$, 29, and 30 respectively. The red lines are based on our $z \sim 9$–10 sample presented here. How well one can expect to resolve the earliest epoch galaxies with future not only depends on the adopted parametrization of size-evolution but the high-redshift normalization.

## APPENDIX
## SIZE EVOLUTION MODEL

Wyithe & Loeb (2011) present a simple model based on the luminosity function slope ($\alpha = 1 - a$) and the size evolution ($m$) to estimate the sizes of galaxies for future observations and observatories. They arrive at a model for the galaxy size which depends on luminosity ($m_{AB}$), redshift ($z$) as follows (their Equation (9)):

$$r_e = R_0 \left( \frac{D_L(z)}{D_L(z_0)} \right)^{\frac{2}{3(1+a)}} 10^{\frac{m_{AB,0}-m_{AB}}{7.5(a+1)}} \left( \frac{1+z}{1+z_0} \right)^{-m}, \quad (4)$$

where $R_0$, and $m_{AB,0}$ are normalization parameters determined at a later epoch ($z_0$). They adopt the mean of some of the Oesch et al. (2009) results. We adopt the $z_0 = 8$ values: $R_0 = 0.4$, $m_{AB,0} = 28.1$, $\alpha = -2.27$ (Bouwens et al. 2014) and $m = -1$ in Figure 3.

For the observatories, they assume diffraction limited observations, i.e.,:

$$\Delta\theta = \frac{1.22\lambda}{D_{tel}} \simeq 0.085 \left( \frac{1+z}{7} \right) \left( \frac{D_{tel}}{2.5} \right)^{-1}, \quad (5)$$

for the wavelength of Ly$\alpha$ and a fiducial $m_{AB} = 28$ source.

Figure 3 shows our comparison to these first expectations to our $z \sim 9$–10 objects. It shows we do slightly better than a simple diffraction estimate because the CANDELS data is drizzled and we have a good PSF model in hand. The model's prediction based on the values above match those of our size measurements for the given AB luminosities.

Starting from the model presented in Wyithe & Loeb (2011), we can extrapolate the $z \sim 9$–10 sample (similar to their Figure 2). Figure 9 shows the model extrapolation from our $z \sim 9$–10

HOLWERDA ET AL.

objects. The simple model from Wyithe & Loeb (2011), suffices to predict galaxy sizes at earliest times, it needs to be anchored to the highest-redshift measurements available if one is to successfully plan observations with future observatories such as *JWST* and ELT (also shown in Figure 3).

Based on the sizes presented in Oesch et al. (2009) ($z_0 = 7$, green lines, $z_0 = 8$ blue lines), one would not have expected *HST* to resolve the fainter of our sources ($m_{AB} \sim 28$). However, with these $z \sim 9$–10 sources confirmed, it appears possible that *HST* may still discover and resolve some rare $z = 10$–11 $m_{AB} = 29$ objects. Conversely, *JWST* and ELT planning will have to take more extended galaxies into account (e.g., NIRspec slit width, etc.).

## REFERENCES

Astropy Collaboration, Robitaille, T. P., Tollerud, E. J., et al. 2013, A&A, 558, A33
Baldry, I. K., Driver, S. P., Loveday, J., et al. 2012, MNRAS, 421, 621
Beckwith, S. V. W., Stiavelli, M., Koekemoer, A. M., et al. 2006, AJ, 132, 1729
Bouwens, R. J., Illingworth, G. D., Blakeslee, J. P., Broadhurst, T. J., & Franx, M. 2004, ApJL, 611, L1
Bouwens, R. J., Illingworth, G. D., Blakeslee, J. P., & Franx, M. 2006, ApJ, 653, 53
Bouwens, R. J., Illingworth, G. D., Labbe, I., et al. 2011a, Natur, 469, 504
Bouwens, R. J., Illingworth, G. D., Oesch, P. A., et al. 2011b, ApJ, 737, 90
Bouwens, R. J., Illingworth, G. D., Oesch, P. A., et al. 2011c, ApJ, 737, 90
Bouwens, R. J., Illingworth, G. D., Oesch, P. A., et al. 2014, arXiv:1403.4295v4
Bouwens, R. J., Oesch, P. A., Illingworth, G. D., et al. 2013, ApJL, 765, L16
Bradley, L. D., Trenti, M., Oesch, P. A., et al. 2012, ApJ, 760, 108
Brammer, G. B., van Dokkum, P. G., Franx, M., et al. 2012, ApJS, 200, 13
Brammer, G. B., van Dokkum, P. G., Illingworth, G. D., et al. 2013, ApJL, 765, L2
Cameron, E., & Driver, S. P. 2007, MNRAS, 377, 523
Capak, P., Faisst, A., Vieira, J. D., et al. 2013, ApJL, 773, L14
Casertano, S., de Mello, D., Dickinson, M., et al. 2000, AJ, 120, 2747
Coe, D., Zitrin, A., Carrasco, M., et al. 2013, ApJ, 762, 32
Courteau, S., Dutton, A. A., van den Bosch, F. C., et al. 2007, ApJ, 671, 203
Curtis-Lake, E., McLure, R. J., Dunlop, J. S., et al. 2014, arXiv:1409.1832
de Jong, R. S., & Lacey, C. 2000, ApJ, 545, 781
Dutton, A. A., & van den Bosch, F. C. 2012, MNRAS, 421, 608
Ellis, R. S., McLure, R. J., Dunlop, J. S., et al. 2013, ApJL, 763, L7
Fall, S. M., & Efstathiou, G. 1980, MNRAS, 193, 189
Feldmann, R., Carollo, C. M., Porciani, C., Lilly, S. J., & Oesch, P. 2011, ascl soft, ascl:1110.005
Ferguson, H. C., Dickinson, M., Giavalisco, M., et al. 2004, ApJL, 600, L107
González, V., Bouwens, R., Illingworth, G., et al. 2014, ApJ, 781, 34
Grazian, A., Castellano, M., Fontana, A., et al. 2012, A&A, 547, A51
Grogin, N. A., Kocevski, D. D., Faber, S. M., et al. 2011, ApJS, 197, 35
Hathi, N. P., Jansen, R. A., Windhorst, R. A., et al. 2008, AJ, 135, 156
Hinshaw, G., Larson, D., Komatsu, E., et al. 2013, ApJS, 208, 19
Holwerda, B. W. 2005, arXiv:astro-ph/0512139
Holwerda, B. W., Trenti, M., Clarkson, W., et al. 2014, ApJ, 788, 77
Huang, K.-H., Ferguson, H. C., Ravindranath, S., & Su, J. 2013, ApJ, 765, 68
Hunter, J. D. 2007, CSE, 9, 90
Illingworth, G. D., Magee, D., Oesch, P. A., et al. 2013, ApJS, 209, 6
Jones, E., Oliphant, T., Peterson, P., et al. 2001, SciPy: Open source scientific tools for Python
Kawamata, R., Ishigaki, M., Shimasaku, K., Oguri, M., & Ouchi, M. 2014, arXiv:1410.1535
Koekemoer, A. M., Faber, S. M., Ferguson, H. C., et al. 2011, ApJS, 197, 36
Laureijs, R., Amiaux, J., Arduini, S., et al. 2011, arXiv:1110.3193
Mo, H. J., Mao, S., & White, S. D. M. 1998, MNRAS, 295, 319
Mosleh, M., Williams, R. J., Franx, M., et al. 2012, ApJL, 756, L12
Oesch, P. A., Bouwens, R. J., Carollo, C. M., et al. 2010, ApJL, 709, L21
Oesch, P. A., Bouwens, R. J., Illingworth, G. D., et al. 2013a, ApJ, 773, 75
Oesch, P. A., Bouwens, R. J., Illingworth, G. D., et al. 2013b, ApJ, 773, 75
Oesch, P. A., Bouwens, R. J., Illingworth, G. D., et al. 2014, ApJ, 786, 108
Oesch, P. A., Carollo, C. M., Stiavelli, M., et al. 2009, ApJ, 690, 1350
Ono, Y., Ouchi, M., Curtis-Lake, E., et al. 2013, ApJ, 777, 155
Peng, C. Y., Ho, L. C., Impey, C. D., & Rix, H. 2002, AJ, 124, 266
Peng, C. Y., Ho, L. C., Impey, C. D., & Rix, H. 2010, AJ, 139, 2097
Pirzkal, N., Rothberg, B., Ryan, R., et al. 2013, ApJ, 775, 11
Planck Collaboration, Ade, P. A. R., Aghanim, N., et al. 2014, A&A, 571, A16
Ryan, R. E., Thorman, P. A., Yan, H., et al. 2011, ApJ, 739, 83
Shen, S., Mo, H. J., White, S. D. M., et al. 2003, MNRAS, 343, 978
Shibuya, T., Ouchi, M., & Harikane, Y. 2015, arXiv:1503.07481
Skelton, R. E., Whitaker, K. E., Momcheva, I. G., et al. 2014, ApJS, 214, 24
Somerville, R. S., Barden, M., Rix, H.-W., et al. 2008, ApJ, 672, 776
Spergel, D., Gehrels, N., Breckinridge, J., et al. 2013, arXiv:1305.5425
Stark, D. P., Schenker, M. A., Ellis, R., et al. 2013, ApJ, 763, 129
Steidel, C. C., Adelberger, K. L., Giavalisco, M., Dickinson, M., & Pettini, M. 1999, ApJ, 519, 1
Stringer, M. J., Shankar, F., Novak, G. S., et al. 2014, MNRAS, 441, 1570
Trenti, M. 2012, in AIP Conf. Ser. 1480, First Stars IV—From Hayashi to the Future, ed. M. Umemura & K. Omukai (New York: AIP), 238
Trenti, M. 2014, in Bright Galaxies at Hubble's Detection Frontier: The Redshift ž9–10 BoRG Pure-Parallel Survey (HST Proposal)
Trenti, M., Bradley, L. D., Stiavelli, M., et al. 2011, ApJL, 727, L39
Trenti, M., Bradley, L. D., Stiavelli, M., et al. 2012, ApJ, 746, 55
van der Wel, A., Bell, E. F., Häussler, B., et al. 2012, ApJS, 203, 24
van der Wel, A., Franx, M., van Dokkum, P. G., et al. 2014, ApJ, 788, 28
van Dokkum, P., Brammer, G., Momcheva, I., et al. 2013, arXiv:1305.2140
Windhorst, R. A., Cohen, S. H., Hathi, N. P., et al. 2011, ApJS, 193, 27
Wyithe, J. S. B., & Loeb, A. 2011, MNRAS, 413, L38
Zheng, W., Postman, M., Zitrin, A., et al. 2012, Natur, 489, 406